Interferometric Study of Plasma Expansion at Early Stages

The energy deposited by a femtosecond (*fs*) laser pulse on a solid target increases the temperature in a well defined region[1], creating, with a threshold of about $10^{11} - 10^{13}$ W/cm^2 [30] a solid density plasma (see Ch.3). As the superficial areas of the plasma start expanding towards the vacuum, the region of transition between the two states propagates deeper in the bulk, at a speed which depends on the initial electron temperature (Fig.4.1).

In this chapter I describe the experiment performed to directly measure the parameters of expansion of this plasma, created by a moderate intensity femtosecond pulse, in a time scale for which the shock area doesn't penetrate more than few microns in the bulk. An Aluminum plasma is produced by a $\tau = 150fs$ laser pulse, whose total energy is comparable to the total energy contained in the prepulse of a standard CPA multi-terawatt laser chain[2]. The density evolution is probed at different delays by a second laser pulse at normal incidence to the main laser pulse. The phase plane of the probe pulse, analysed by interferometry, is used to reconstruct the electron density map.

The searched timescale ($t < 100ps$) corresponds, according to hydrodynamic simulations, to the time taken by the shock to propagate over $2\mu m$.

The final comparison between experimental results and simulations allows us to follow the evolution of the plasma expansion and to infer the properties of the shock wave in the dense part of the target.

[1] In *fs* regime we use $\delta_l = c/\omega_{pe}$ as expression for the skin depth, since at room temperature, all other collisional phenomena have timescales longer than the pulse duration.

[2] Considering $contrast \cdot intensity \cdot \pi w_0^2 \cdot \tau_{ASE} = 10^{-6} \cdot 10^{19} \pi \left(3 \cdot 10^{-4}\right)^2 \cdot 3 \cdot 10^{-9} = 15mJ$.

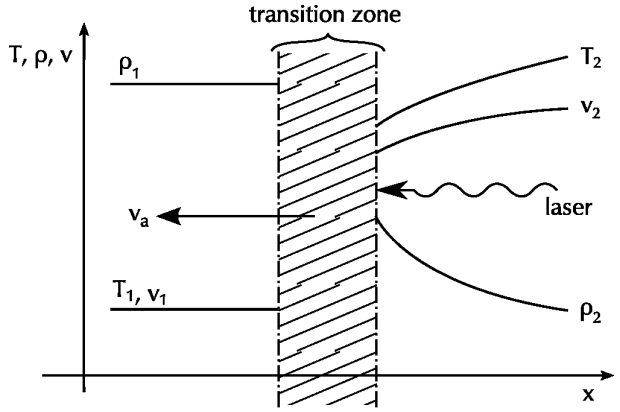

Figure 4.1: General scheme of the expansion of a solid target following laser irradiation. A transition area propagates through the unperturbed (ρ_1, T_1) bulk; a density gradient ($\{\rho_2, T_2, v_2\}(x,t)$) is formed and expands from its right surface. (Adapted from [22])

4.1 Experimental Setup

The experiment is a *pump/probe* experiment, where two separate beams from the same laser source are used, one to produce the physical situation and the second to measure the obtained parameters. This kind of experiment enables the user, given a sufficient repeatability, to measure the fast evolution of phenomena with a temporal resolution that is limited only by the duration of the probe pulse. This kind of approach is one of the key features of short pulse lasers and is possible when the duration of the probe beam is shorter then the timescale of the probed phenomenon.

4.1.1 Laser

For this experiment I used the *Salle Verte* laser facility. This is a CPA based laser system, whose basic scheme is depicted in Fig.4.3. The initial pulse is produced by a Ti:Sa crystal pumped by a CW Argon source. The repetition rate is lowered to $10Hz$ and the pulse stretched to $400ps$. Two, Nd:YAG pumped, multipass amplification stages, a 8-pass and a 4-pass, boost the single pulse energy up to $100mJ$. At this point, a birefringent window is used to rotate the beam polarization and a polarizer to split the two components in two different beams, before compression. Two independent grating compressors are then used to compress the pulses, giving two beams of $150fs$ pulses at a repetition rate of $10Hz$. The total energy after compression contained in the two

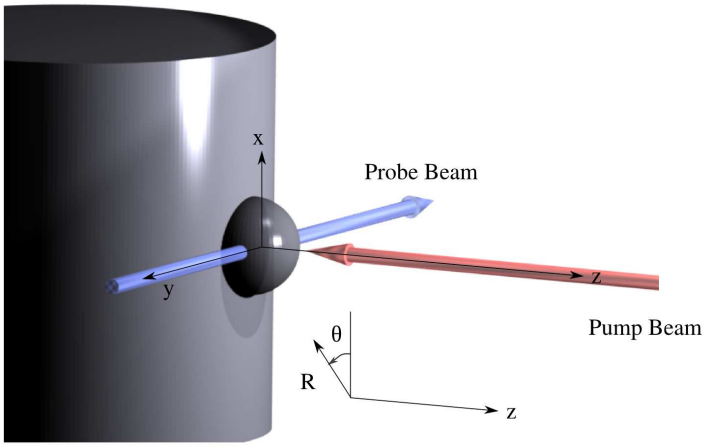

Figure 4.2: Experiment Layout

synchronized[3] pulses is about $50mJ$; the user has the freedom of changing the angle of polarization before the compression stages, deciding the ratio of energy to be sent to each beamline. The difference in optical path between the two lines is roughly $3m$ at the moment they arrive in the experimental room, having the *probe* pulse in late of about $10ns$. The laser beam is a gaussian beam with diameter of $2w = 25mm$. One of the two

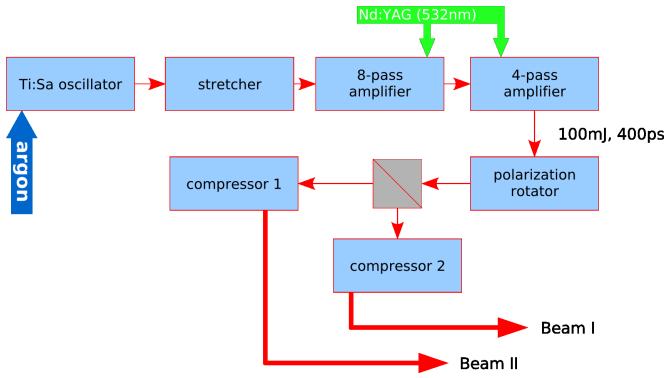

Figure 4.3: Scheme of the CPA laser chain in Salle Vert, LOA

compressors is found to have a lower efficiency so that a energy loss is introduced on one of the beamlines. In order to maximize the available energy on the *pump* beamline, the lower efficiency compressor is used on the *probe* beamline.

[3]The two compressed pulses are produced by a single pulse before compression.

4.1.2 Experiment

A brief scheme of the optical system for the plasma interferometry experiment is shown in Fig.4.4.

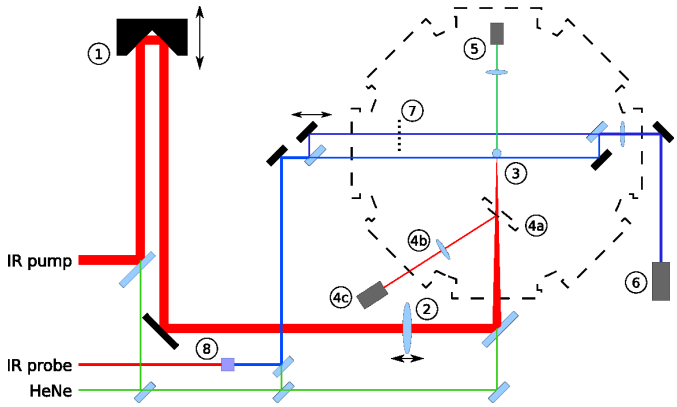

Figure 4.4: Scheme of the experiment: 1. delay line; 2. main focusing lens; 3. target; 4a-c analysis of the focal spot, including flipping mirror, microscope objective and camera; 5. imaging of lateral displacement of the target; 6. 12*bit* camera to record the interferograms; 7. shutter; 8. BBO crystal.

Pump beamline

The delay line (Fig.4.4-1) is made of two mirrors glued on a metal support to form 90^o one to the other and mounted on a step-by-step micro-controlled motor with $1\mu m$ wide steps. The motor itself is mounted and carefully aligned on a $1m$ long rail to give freedom of setting the relative delay between the two pulses.

The *pump* beam is sent to a singlet lens $f = 100cm$ (Fig.4.4-2) which focuses the beam on the target; in the ideal case (beam waist on the lens) it would produce a spot of $2w_0' = 40\mu m$ (eq. (2.7)). The focal spot is imaged by the microscope objective on the 12*bit* CCD camera (Fig.4.4-4bc) with a resolution of $0.43\mu m/pix$ [4] and the tilting of the lens is corrected to minimize astigmatism. The analysis of the focal spot (Fig.4.5) shows that the energy within the FWHM contour (marked in blue) is the 26% of total. The ratio is calculated numerically by subtracting the measured background and integrating the contoured area. There is a non-negligible amount of energy in the satellite, clearly visible in the upper-right corner. It was not possible to eliminate it by acting on lens

[4] The effective magnification is $\approx 23\times$.

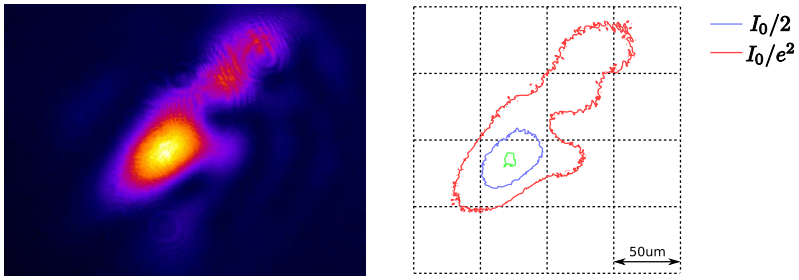

Figure 4.5: CCD image and intensity contours of the focal spot

or microscope alignments, so that we believe it to be caused by inhomogeneities on the phase front. For this experiment no adaptive optics were available to correct the phase front of the laser beam.

In the final configuration the total per-pulse energy after compression is $35mJ$; given a 59% of energy in the $2w_0$ contour (Fig.4.5-red with the satellite cut out) the resulting flux on target is $I_0 \approx 4 \times 10^{15} W/cm^2$.

Probe beamline

In order to probe higher densities in the plasma the *probe* laser beam is doubled in frequency, by a type-I BBO crystal of $2mm$ in thickness (Fig.4.4-8). Having the frequency of the *probe* different from the one that creates the plasma is also necessary to be able to filter out all the light at the *pump* wavelength being diffused during the interaction, and to produce cleaner interferograms.

It has to be underlined that the doubling process reduces the spectral content of the input pulse and acts on the spectral phase, due to different matching conditions for the various spectral components. Our input pulse has a duration $\tau = 150fs$ which corresponds, for an ideal gaussian pulse, to a spectral bandwidth of $\Delta\lambda = 12.6nm$; simulations showed that the doubled pulse will have a duration between $400fs$ and $500fs$.

Interferometry

The interference is realized in a Mach-Zender (MZ) setup. The first two components, one beam splitter and one mirror, can be seen on the same figure outside the chamber,

on the left side, and the other two on the rightmost part of the chamber itself. Hereby for the rest of this chapter, when talking about the beams inside the interferometer optics, I will distinguish the two as *probe* and *reference*, where the *reference* beam is the part of *probe* reflected by the first beam splitter and not interacting with the plasma. The

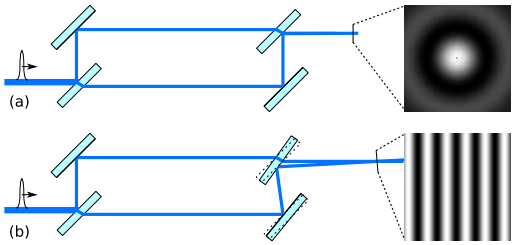

Figure 4.6: Mach-Zender interferometer setup (a); if the superposition of the two beam on the second beam splitter is done off-axis, a transverse carrier frequency appears (b).

output part of the setup is tilted, to produce a carrier frequency on the recombination of the two beams: the tilt is regulated to produce the smallest inter-fringe on the horizontal direction and to void it on the vertical. Also, the sign of the angle between the two beams is chosen so that a phase anticipation on the *probe* ($v_{phase,plasma} > c$) produces fringes *moving away* from the target shadow, and not entering it. A deeper discussion about the importance of a spatial carrier frequency is presented in section Ch.B.
A micrometric control is placed on the first mirror to be able to correct one of the MZ legs and the temporal superposition of the two pulses coming from the two parts (the probe and the reference); being $\tau_{probe} = 500fs$ the superposition will hold over a $\Delta z = 150\mu m$ wide interval[5]. The *reference* beam can occasionally be intercepted to produce a shadowgram of the target.

Imaging

The experimental information, as a phase perturbation on the *probe* beam in the MZ setup, is produced when the beam propagates through the plasma plume. In order to *transport* at its best the phase plane as it were when perturbed, a lens is inserted between the plasma and the imaging device. The first aim is to conjugate the plane orthogonal to the *probe* propagation direction and passing through the target normal (object plane) to a plane outside the interaction chamber; the second aim is to introduce

[5]The position of this mirror has to be changed when pumping down the chamber.

a magnification.
Some important choices were done about the configuration of the imaging system. First of all a focal as short as possible is to be preferred, in order to keep the lens as small as possible and to achieve the biggest numerical aperture. On the other hand a certain distance is to be kept between the Mach-Zender components and the interaction point; otherwise the metal ablation process would result in deposit of the ablated material on the optics, with a consequent degradation of the optical surfaces' quality. One should also avoid to have the object plane imaged through a beam splitter, as the thick, tilted, slab of glass between the lens and the object introduces uncorrectable geometrical aberrations.

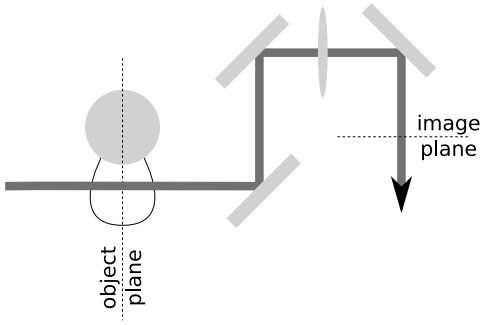

Figure 4.7: Scheme the imaging part on the plasma probe

Balancing all these factors, an achromatic doublet of $\phi = 50mm$ diameter and $f = 19cm$ (Fig.4.7) is chosen. The minimum distance from the interaction point we could place it is lower than $x = 21cm$. From the geometrical optics formula it conjugates to a plane at $380cm$ and produces a magnification $> 10\times$. The diffraction limit, calculated as

$$d = \frac{\lambda}{2n \sin(\theta)} \tag{4.1}$$

(where $\theta = \arctan[\phi/2x]$, being ϕ the lens diameter and x the object distance) turns out to be $\delta_x = 1.5\mu m$. Unfortunately this configuration (Fig.4.7) limits the freedom in the spatial carrier frequency. In fact, after having correctly aligned the lens for the *probe* side, the angle between the beams can be regulated only on acting on the far side (Fig.4.6) of the Mach-Zender, the beam-splitter and the mirror. The two beams finally

superpose on the chip of a $12bit$ linearized camera[6]. The final measured magnification on the imaging of interferograms is $m = 12.85\times$, giving a resolution of $0.77\mu m/pix$.

Target

The target is composed by an array of $200\mu m$ thin metal (Aluminum) wires. The choice fell on cylindrical target because of *(i)* their ease of alignment and *(ii)* to probe the density profile near the critical density without being masked by the rest of the target. The *probe* beam will always be tangent on the target surface and its perpendicularity to the main plasma expansion direction, i.e. the *pump* laser direction, is set by geometrical constraints of the optical setup and the target wire lateral placement. For the alignment procedure, see section 4.2.1. The holder itself is mounted on a three axis micro-controlled

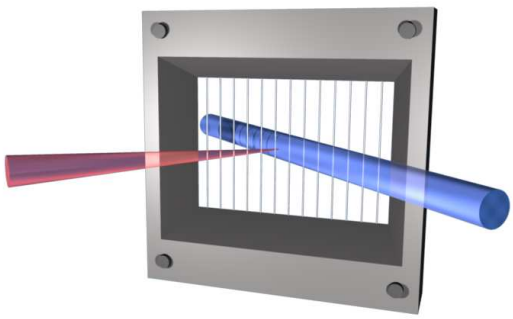

Figure 4.8: Target holder and wires; more than one pump shot was possible on a single wire, as the laser damage was not deep enough to break it.

set of motors for focusing, lateral and vertical displacement.

4.2 Experimental Procedure

The self-consistency of the entire set of data in this experiment strongly relies on the best reproduction of the system configuration for every delay. It has to be stressed that having the delay line on the *pump* beam makes the system more critical, requiring additional work and lateral realignment of the target for every important change on the delay line.

Another important parameter is the synchrony between the *pump* and the *probe* pulses. In fact, the zero point on the plasma's timescale is set by the arrival of the *pump* beam.

[6]PCO PixelFly, 12bit, 640×480 pixels of $9.9\mu m \times 9.9\mu m$.

Since I want to characterize the plasma's evolution on the absolute scale of times with its zero on the moment the expansion starts, it is necessary to carefully calibrate the optical path of the two beamlines.

4.2.1 Spatial alignments

At first the Mach-Zender components and the focusing lens are placed, in a way that the focal point of the lens is almost centered in the *probe* beam profile. The relatively long focal length eases the alignment, being the Rayleigh range $z_0 = 6mm$. At this point of the procedure a precise positioning of the *pump* spot in the *probe* beam is not fundamental, given the diameter of this last.
The imaging system on the *probe* beam path (lens and camera) is then aligned. A white, incoherent, light source is used as an object, put at the intersection between the *pump* and the *probe* axis. The target is finally put in its place, in the supposed best focus position and at the center of the *probe* beam.
The fine alignment of the target in the *pump* focus is accomplished by looking in real-time at shadowgrams[7]. A small plasma structure is formed on the target surface by the strongly attenuated *pump* beam and observed on the imaging device; if the *pump* focusing lens is moved along its axis with the micrometric translation, a range is defined where the intensity is above the threshold for target ionization, which makes a bubble visible in the target shadowgram. As neutral densities are added in the front of the focusing lens, this range becomes smaller and smaller. The procedure is stopped when this range is smaller than $200\mu m$. This position of the target is taken as a reference on the shadowgram and used to align forthcoming targets on the *pump* focal plane.
The target is also moved on its horizontal axis to keep the imaged bubble as big as possible, thus ensuring the correct lateral positioning. The reference for the lateral position is taken by the camera Fig.4.4-5 on the shadow of the target, illuminated by a HeNe laser collinear to the *pump* beam.

4.2.2 Synchrony

The delay line must be regulated to temporally superpose the two pulses, *pump* and *probe*, on the target. This condition is searched by substituting the target holder with a thin glass blade ($150\mu m$ thick) acting as a beam splitter and sending the two beams together on the lateral alignment camera. The delay line is then moved until the in-

[7]Shadowgrams are obtained by obstructing the *reference* beam in the MZ.

terference condition is produced. The interference pattern is observable within a range of $\approx 600\mu m$ on the delay line. To carry out this measurement the BBO crystal was removed.

4.2.3 Error Estimation

Two kinds of errors are introduced in the experimental procedure: the alignment of the targets and the numerical analysis of the interferograms. The second type is explored in Annex.B and it proved to be negligible when compared to alignment errors.

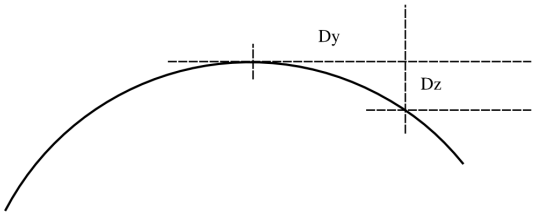

Figure 4.9: Geometrical relationship between a lateral misalignment of the target and the position of its surface on the *pump* axis.

Spatial errors

The uncertainties on the target position (Fig.4.9) are concentrated on lateral and focus alignments. A lateral misalignment would result in a surface, as seen by the *pump* pulse, with a tilt, which means a different direction of plasma expansion. Not considering the difference in physical situation (for example the loss of cylindrical symmetry seen by the *probe*), the result would be in higher density regions seen nearer to the target surface. Considering that on the lateral alignment camera the target boundary is seen with a resolution better than $1\mu m/pix$, a misalignment $10pix$ would have a negligible consequence on the final result.

The positioning in focus, where the reference is seen on the shadowgraphy on the interferogram camera, is more important, as a misalignment here, while not affecting the physics of the interaction, would directly result in a wrong measure of the distance between a given density and the original surface. In the alignment of a new target, uncertainties are introduced by diffraction effect on its boundary (see Fig.4.10a): its

position in z can be defined in a range of $\pm 4pix = \pm 3\mu m$. I use this quantity as the uncertainty on the z value of experimental measurements.

Temporal errors

As introduced in 4.2.2, the temporal superposition of the beams is defined down to $600\mu m$ on the delay line. This range introduces a systematic uncertainty of $\pm 2ps$ on the temporal axis. Aside of this, every movement of the delay line has a precision of $\approx 1\mu m$, which introduces a negligible error of $\pm 4fs$.

4.3 Experimental Data

For each delay time, four images need to be taken, namely a shadowgraphy before (Fig.4.10a) and after (Fig.4.10d) the *pump* shot, a reference interferogram (Fig.4.10b) and the interferogram with the plasma (Fig.4.10c). The procedure is repeated at least twice for delays between $0ps$ and $100ps$, by steps of $3ps$.

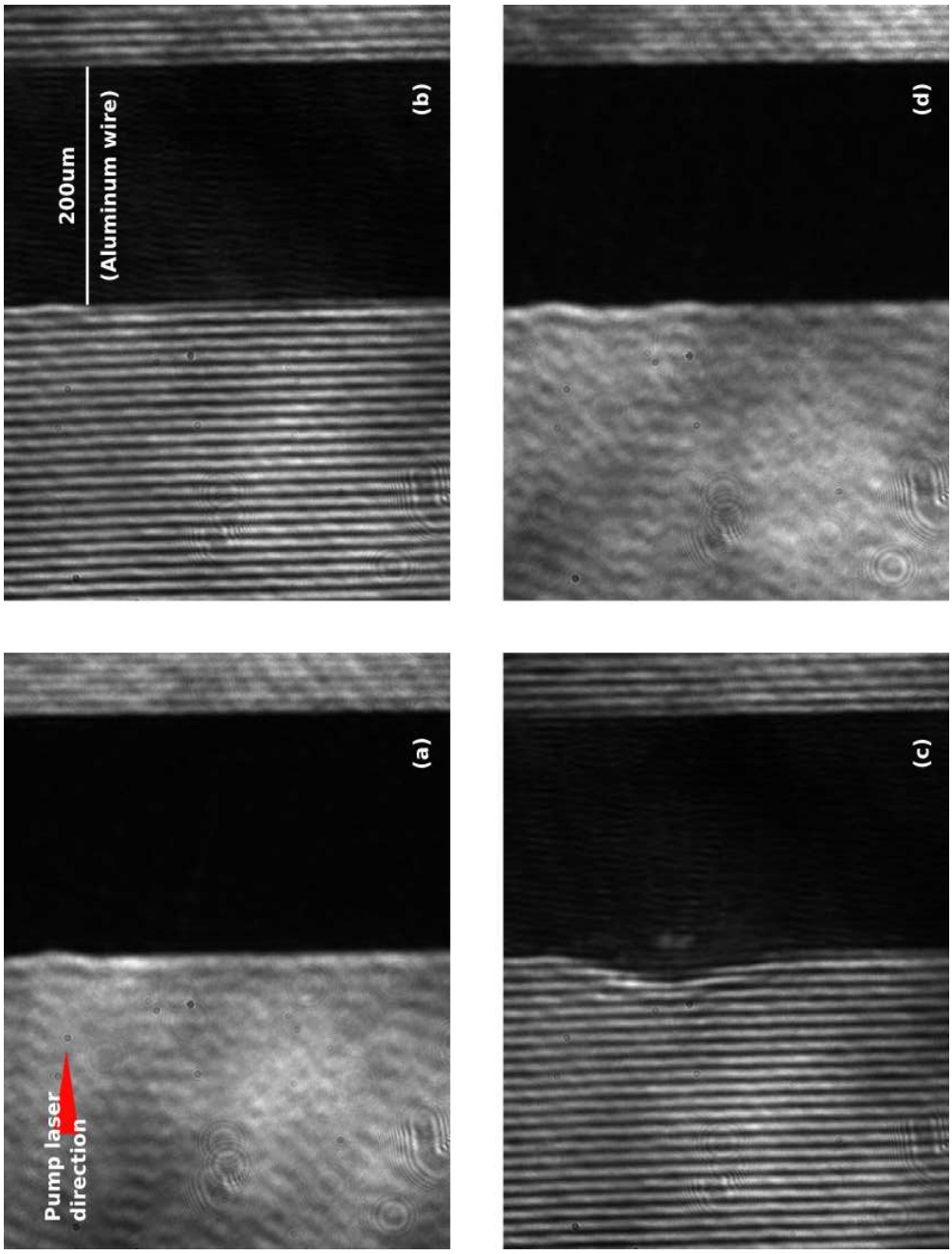

Figure 4.10: A set of images recorded for a single delay ($t = 90ps$). (a) Shadowgraphy before the *pump* shot; (b) reference interferogram; (c) plasma interferogram; (d) shadowgraphy after the shot, the hole is clearly visible on the left side of the target. (Images have a resolution of $1.2\mu m$; inter-fringe is $\lambda_{het} \approx 10\mu m$)

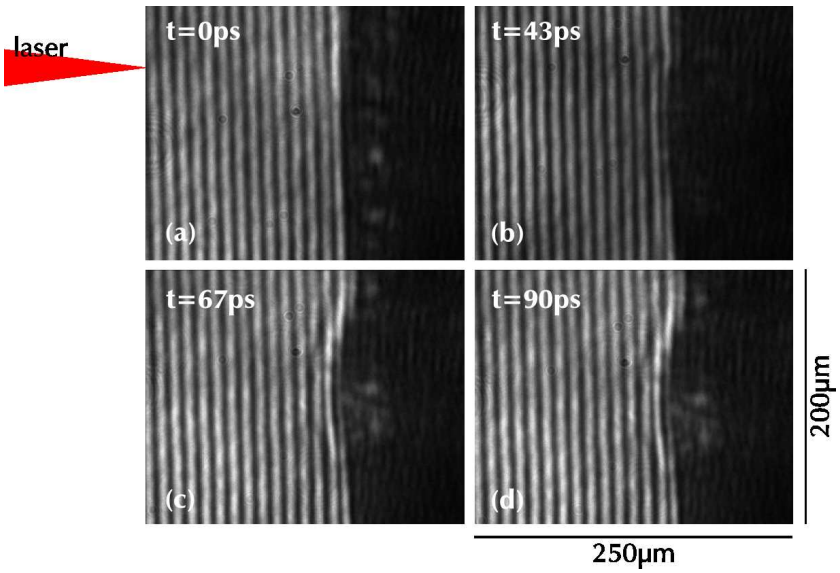

Figure 4.11: Plasma expansion at four different delays : (a) 0ps, (b) 43ps, (c) 67ps and (d) 90ps.

As the delay line is moved, a black bubble is seen to form, starting $6-7ps$ later than the *pump* pulse and to expanding as time passes. The black area, where complete absorption or deviation of *probe* happens, is surrounded by deformed fringes. In Fig.4.11 interferograms recorded at different times are shown.
The interferograms are filtered and the phase map is calculated and inverted to obtain the 2D density map (see Ch.B). The filtering process is accomplished in the Fourier space by limiting the information that is contained in the image to certain physical constraints, like the size of the focal spot and the parameters of the optical system that created it (see B.2.1 for details).
The phase map is reconstructed from the filtered image and the heterodyne carrier removed by 2D linear fit on the phase plane[8].
On behalf of cylindrical symmetry of the created plasma, the symmetry axis (Fig.4.12-*upper*) is searched on the phase planes and the phase cuts on $\phi_{exp}(x, z = constant)$ are symmetrized by averaging the two halves. The obtained phase matrix is inverted from (x, z) to (r, z) by the Abel formula (4.2)-I and electron density calculated by (4.2)-II.

[8] If the phase on the interferogram is represented by $\Phi(\underline{x}) = \underline{k}_{het} \cdot \underline{x} + \varphi(\underline{x})$, the heterodyne component $|\underline{k}_{het}| = 2\pi/\lambda_{het}$ can be removed by directly subtracting the $\underline{k}_{het} \cdot \underline{x}$ plane.

$$\begin{cases} \left(\dfrac{\partial\phi}{\partial r}\right)(r,z) &= -\dfrac{1}{\pi}\displaystyle\int_r^{r_0} \dfrac{\partial\phi_{exp}/\partial x}{\sqrt{x^2-r^2}}\mathrm{d}x \\ n_e\,(r,z) &= \dfrac{m_e\epsilon_0 c^2}{e^2}\left[2k_0\left(\dfrac{\partial\phi}{\partial r}\right)+\left(\dfrac{\partial\phi}{\partial r}\right)^2\right] \end{cases} \tag{4.2}$$

The latter – see (B.19) – makes use of the dependence of the refraction index on the electron density for transverse *em* waves in a cold plasma. The analysis of the entire

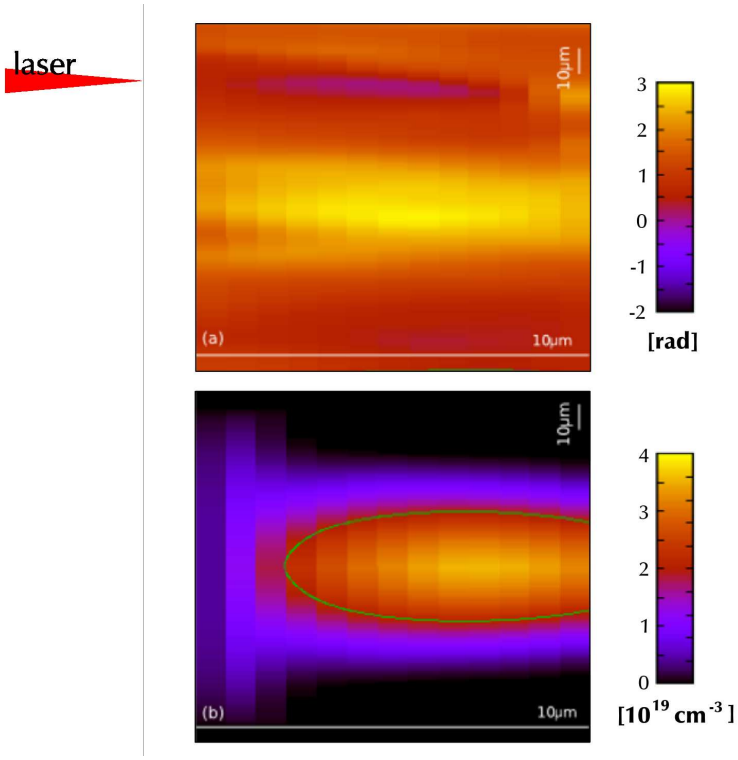

Figure 4.12: 2D map of plasma expansion at a delay of for $\Delta t = 67ps$ (Fig.4.11c); (a) phase map from the interferogram; (b) density map after Abel inversion (green line represents the isodensity contour at $n_e = 2 \cdot 10^{19}\, cm^{-3}$).

collection of images provides the set of 2D maps of electron densities from $6ps$ to $100ps$. The set of measured densities ranges between $2 \times 10^{18} cm^{-3}$ and $4 \times 10^{19} cm^{-3}$. The error introduced by the phase retrieval process, propagated through the Abel inversion – (B.29) – results in uncertainties on the density values in the range of $10^{12} - 10^{13} cm^{-3}$, which are smaller than other sources of uncertainty.

4.4 Results and Comparison with Simulations

Simulations

Within the timescale we measured the plasma expansion, its longitudinal dimension (z) remains small compared to the focal spot size. We can then neglect transversal (r) expansion and simulate the plasma expansion with the 1D1/2 Lagrangian hydrodynamic code Chivas. It is a mono-dimensional cylindrical code where the meshes have a time dependent transverse size, expanding radially with a velocity that depends on the pressure and density existing in the cell[44]. This code is adapted to short pulse laser-matter interaction by solving the Helmholtz equation[9], and it includes the Nohel code, which is an atomic physics model used to describe the ionization, the equation of state and the opacity of matter. For numerical convenience, we have considered a thinner Aluminium target ($8\mu m$). Since the shock wave propagates only over $2\mu m$ inside the target after $100ps$, we are confident that our numerical results can satisfactory be compared with the experimental case ($200\mu m$). This bulk material is irradiated by a laser pulse which has a temporal FWHM of $150fs$ and a focal spot of $40\mu m$ containing $16mJ$ of energy. The code simulates as well the propagation of a transitional zone – shock wave, showing a density higher then the solid density of the target – between the unperturbed material (towards the inner part of the target) and the "ablation front" where the high temperature results in the production of a plasma bubble, which expands towards the vacuum (Fig.4.1). The code is able to simulate correctly the rarefaction until a density of $10^{19}cm^{-3}$.

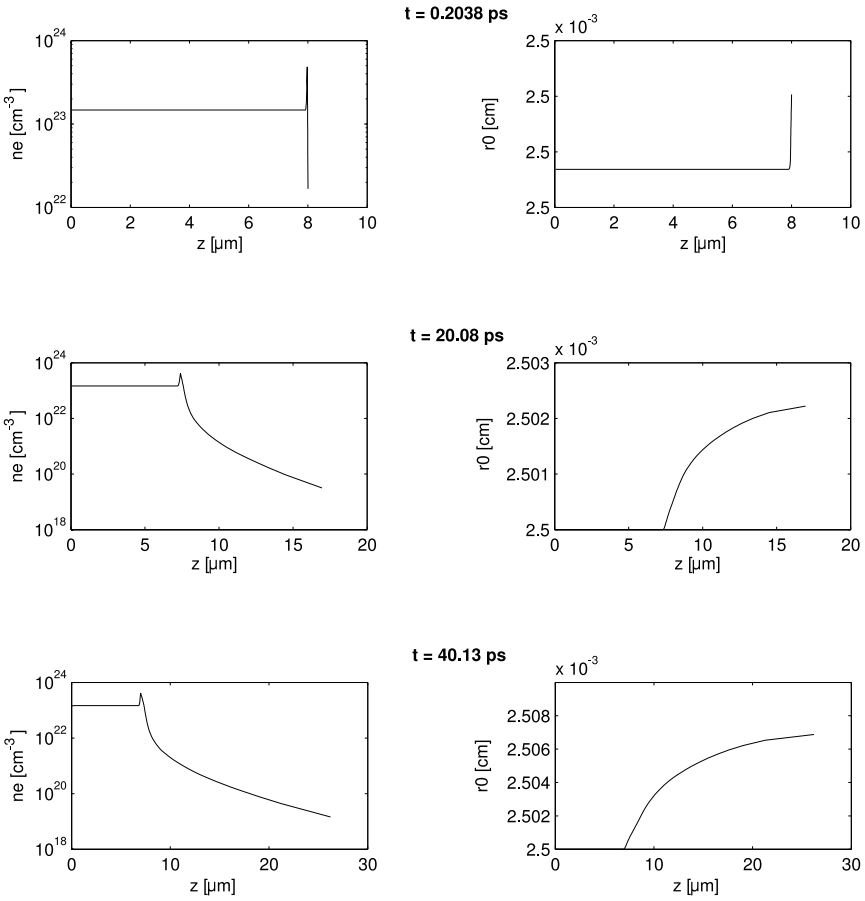

Figure 4.13-a: Chivas simulations for the plasma plume produced on an Aluminum target by a $\tau = 150fs$ long laser pulse (coming from the right to the left) with $16mJ$ of energy in a gaussian spot of $50\mu m$ FWHM diameter. The initial, unperturbed target boundary is at $z = 8\mu m$. At $0.2ps$ the laser pulse is over and the shock is created. On the left it is shown the density decreasing from the bulk density (left side of the plot) towards the vacuum (right side). On the right, the transverse size (radius) of the plasma plume.

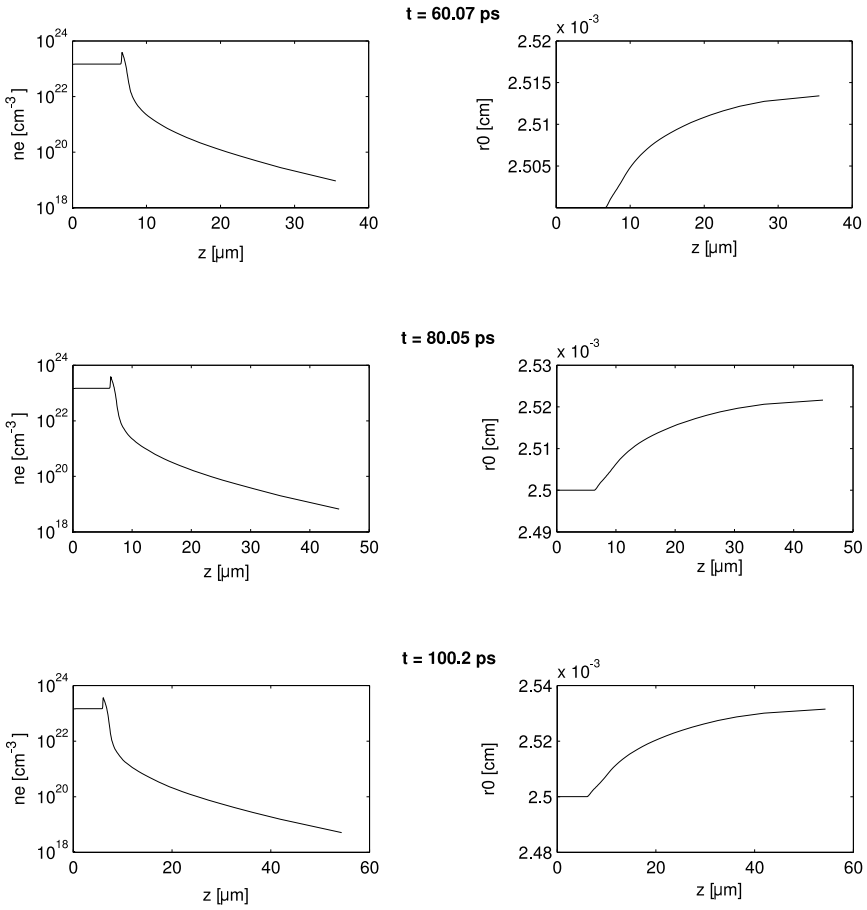

Figure 4.13-b: (*cont. from Fig.4.13-a* for times from 60*ps* to 100*ps*). For the entire time range the transversal growth is negligible if compared to the propagation over $z-$axis. This confirms the use of $1D\,^1/_2$ simulation code.

At $t = 0ps$ the laser pulse starts to heat the electrons in the target; its interaction with the bulk stops at $t = 0.2ps$. The maximum reached temperature is $\approx 250eV$. At this point a corona starts to expand and the shock wave to penetrate deeper in the bulk. After the first $20ps$ a significant plume is already visible. The simulation is stopped at $t = 100ps$: by this time the shock has penetrated $\approx 2\mu m$ of material, while the plasma front (at the lowest density considered by the code) has reached $\approx 60\mu m$ from the target.

Comparison with experimental data

The simulated data spawns over a density range that is bigger than what experimentally measured. Neglecting what is situated (in the simulations) beyond the $8\mu m$ boundary, not visible by the *probe* beam because masked by the "walls" of the crater, the densities in the plasma gradient range between $n_e = 10^{23}\, cm^{-3}$ to $n_e = 10^{19}\, cm^{-3}$. The critical density for the *probe* beam is $n_{c,400nm} = 6.88 \times 10^{21}\, cm^{-3}$ which is in contrast with the maximum density measured on the interferograms of $\approx 4 \times 10^{19}\, cm^{-3}$. There are many possible reasons for this value being $\ll n_c$. First of all, the entire region with densities between the critical density at $400nm$ and the highest measured density has a maximal length (from simulations) of $\approx 7\mu m$, which corresponds to $3/4\, \lambda_{het}$([9]) on the interferogram; this means that the information on two orders of magnitude in electron density is contained in a deformation of just half a fringe. On the other hand, the attenuation of the beam, while travelling through high density regions, significantly worsen the contrast and the signal to noise ratio, making that part of the interferogram more difficult to analyze. See for example the weak contrast of the rightmost perturbed fringe in Fig.4.11c and Fig.4.11d.

By plotting the simulated density with experimental data (like in Fig.4.14) we find the superposition to be fair, confirming the correlation between the measured densities and their distance from the target. The correlation is even more clear looking at the plot of the propagation, in time, of a test density in comparison with the simulated expansion (Fig.4.15).

[9] The heterodyne spatial wavelength.

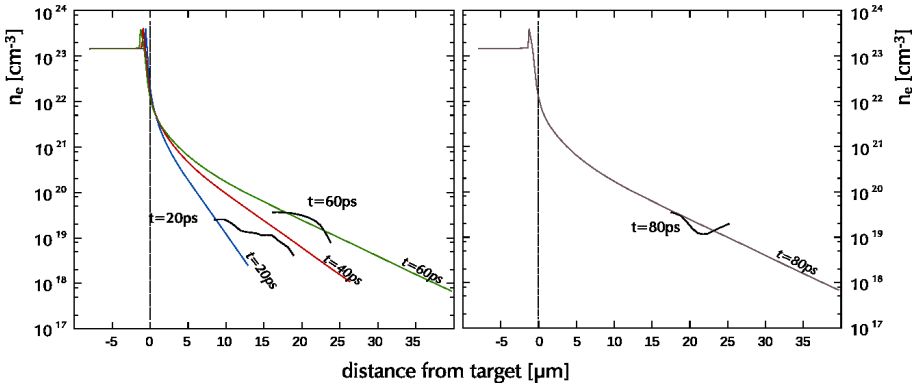

Figure 4.14: Electron density on the symmetry axis vs. distance from target at three different times: (a) 20*ps* (40*ps* dotted), (b) 60*ps* and (c) 80*ps*. Dotted vertical line is the unperturbed target boundary, laser is coming from the right.

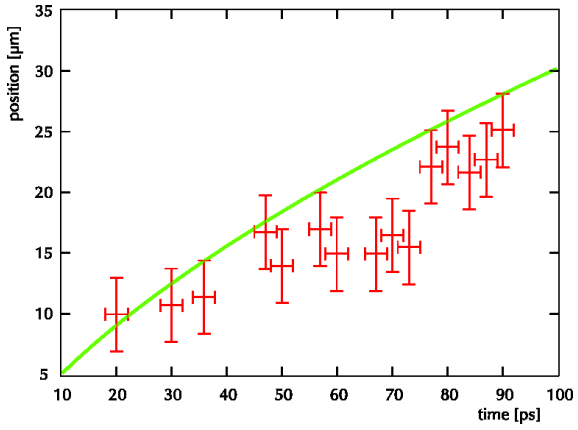

Figure 4.15: Propagation of a constant density front ($n_e = 2 \times 10^{19} cm^{-3}$); the solid line represents the extrapolation from simulated data, crosses are experimental data. Error bars are from alignment uncertainty (see 4.2.1, 4.2.2).

From the simulated density profiles we gain informations concerning the position of the front at the critical density and the gradient length in front of the target (Fig.4.16-*left*). Moreover we can follow the propagation in time of the shock inside the bulk material (Fig.4.16-*right*).

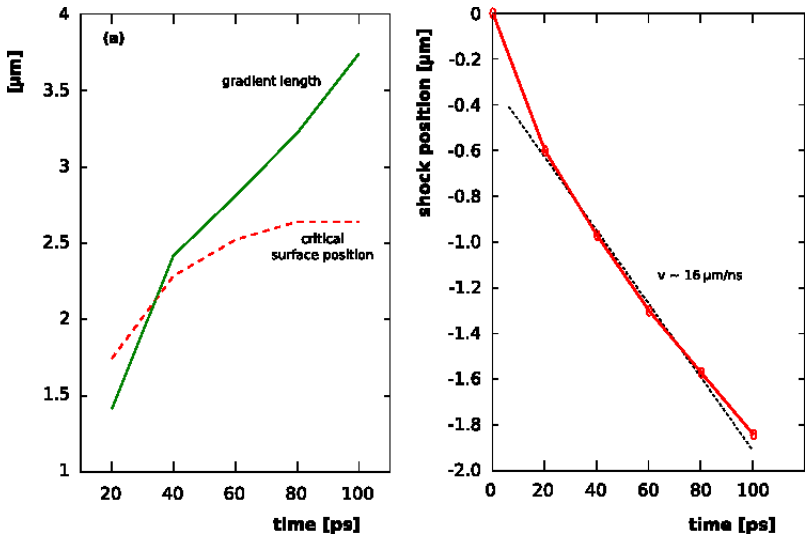

Figure 4.16: Temporal evolution of the plasma profile: *(left)* the dotted line represents the propagation of the critical density front ($n_c = 1.72 \times 10^{21} cm^{-3}$, for $\lambda = 800nm$); the continuous line represents the gradient length (evaluated between n_c and n_c/e); *(right)* propagation of the shock wave in the bulk material (0 marks the position of the target surface before interaction).

4.5 Discussion and Conclusion

The superposition between the simulated density profiles and on-axis experimental points is rather good, see for example Fig.4.15, confirming the correct 1D modelling of plasma expansion at short times. Further data analysis (not reported) also shows the lateral expansion to be negligible within the first $150ps$. The set of density that could be experimentally probed is limited, on the upper side, to $\approx 4 \times 10^{19} cm^{-3}$.

The simulations also show the propagation of the shock wave in the bulk (see the over-density peaks in Fig.4.14, left of the unperturbed boundary). If we plot shock the position versus time (Fig.4.16b) we distinguish two propagation regimes. At the beginning, during the first $20ps$ the shock wave rapidly propagates inside the target and then

reaches a stationary regime. When the measurement timescale becomes much greater than the laser duration, an almost constant velocity is observed; a linear fit gives a velocity of $v = 16\mu m/ns$. If we consider the shock wave behaviour to be independent on the target thickness, the plot in Fig.4.16b enables us to estimate the time at which the shock would reach the rear side of a thin foil. For example, we observe that a target $1\mu m$ thick target would be completely traversed in about $41ps$.

Looking at the gradient length (defined as the distance needed for the electron density to drop of a factor $1/e$ from the critical density for $\lambda = 800nm$) in Fig.4.16a, we find a similar behaviour; after the first $40ps$, when the density profile expands to about $2.5\mu m$, the scale expansion continues at a velocity of $v_{exp} = 20\mu m/ns$. This expansion velocity corresponds to the sound velocity of a plasma heated to $20eV$, which is in agreement with the temperature evaluated numerically.